Research article

Optimization of cantilever piezoelectric harvester to triangular shape with material reduction using finite element analysis

Claudia Săvescu [a,b,*], Daniel Comeagă [b], Adrian Stoicescu [a]

[a] Romanian Research and Development Institute for Gas Turbines COMOTI, Bucharest, 061126, Romania
[b] National University of Science and Technology Politehnica Bucharest, 060042, Romania

ABSTRACT

The paper studies the piezoelectric output performance of a piezoelectric harvester with four piezoceramic layers, assessing if the piezoelectric material can be reduced. The shape optimization regards cantilevers with trapezoidal or triangular longitudinal sections, maintaining comparable electric response with the original rectangular structure. The piezoelectric material is subjected to maximum mechanical stress in the fixed constrained area, decreasing gradually down to null stress towards the free tip. It is worthwhile to study if the material reduction would result in an increased effectiveness in terms of voltage output per unit volume of piezoelectric material. The simulations conducted in COMSOL Multiphysics employ Structural Mechanics – Piezoelectric Devices module, in a Multiphysics approach through Piezoelectric Effect, coupling Solid Mechanics with Electrostatics. It was found that the electric response increases per unit volume of piezoelectric material in triangular configuration with material reduction. A comparable voltage output is obtained after reducing the amount of piezoceramic material towards the free tip, while using an inertial mass of the same value. Hence, the piezoelectric material is used more effectively in the case of triangular cantilever with material cutdown than the traditional rectangular shaped cantilever. The paper also addresses shape optimization while maintaining the same mechanical stress, studying the response when increasing the tip mass for the purpose. All the structures render an even more significantly increased power output for matching optimum load resistor.

1. Introduction

The piezoelectric technology offers wide perspectives as an alternative energy source for a various range of low power applications, from industrial use to smart cities and biomedical applications [1–7]. However, the technology has not yet reached maturity, and most researchers are seeking methods to optimize the electric response by any possible means [8–25].

Optimization is ultimately essential as power-to-size ratio, to improve the piezoelectric output and conversion efficiency while reducing size and utilizing less material more effectively. Various shapes have been studied in the literature, such as circular, rectangular, triangular, trapezoidal, L-shape, E-shape, V-shape, etc. [26–34]. Optimizations of the material and of the effectiveness of piezoelectric harvesters can be studied using finite element method (FEM) software by optimizing the shape and size of the cantilever [35].

The specific literature on triangular and trapezoidal shape optimization is briefly summarized in the following. Chen et al. [26] conducted a numerical assessment validated experimentally on rectangular, trapezoidal and triangular piezoelectric cantilevers, and showed that the triangular structure is the most efficient in terms of voltage output and strain distribution at resonance conditions,

with no inertial mass added. Five cantilever shapes were analysed numerically by Mohamed et al. [27]: T-shaped, L-shaped, rectangular, with variable width, and triangular, without additional tip mass. However, the comparison is not very relevant since the T-shape and the L-shape have geometrically embedded inertial masses and any extra material added to the tip would increase the displacement and strain, and hence the electrical output. Moreover, the triangular shaped beam has the lowest tip material weight, which cannot spotlight its superior effectiveness without additional tip mass. An analytical approach of a tapered beam is proposed by Salmani et al. [28], with inertial mass. The experimental reference for comparison is a rectangular structure, similarly to the paper herein. However, the authors modify several parameters at the same time (tapering, thickness and tip mass), the aim being a structural optimization relying on the best combination of several geometrical parameters.

Benasciutti et al. [30] assessed rectangular, trapezoidal and reverse trapezoidal shapes analytically and numerically. The authors evaluate a dimensionless stress, by maintaining the same inertial load due to the proof mass, but they do not specify any values for the reference stress, inertial force or tip mass. Besides the plotted nondimensional values that cannot be related to a certain quantity, it is asserted that the reversed trapezoidal structure provides a large stress concentrated at the fixed constraint, and the highest stress values may exceed the ultimate tensile strength. Even though the experimental tests do not resemble the simulated geometries, the authors discard the reversed trapezoidal case, as the trapezoidal shape has a more uniform distribution and lower maximum stress. Baker et al. [36] compared a custom-ordered triangular PEH to a rectangular one, claiming a 30 % power output increase. Unfortunately, the experimental paper does not provide specific values for any output parameters to support the percentage increase. Interestingly, the authors claim that, in order to ensure a fair comparison, they kept equal all of the following: piezoelectric material volume, inertial mass, natural frequency and maximum strain, which makes the paper scientifically unreliable without providing any proper measured values. The inertial mass of the rectangular structure is much wider than triangular structure's tip mass, and no dimensions, density or weighting are provided.

Even though papers regarding this topic and geometrical improvement to trapezoidal/triangular shape have been emerging lately, a valid evaluation in the same mechanical stress conditions between various shapes has not yet been addressed in any of the existent published literature, to the authors' knowledge.

The mechanical stress is being evaluated in this paper, as it is a crucial parameter, since subjecting the structure to high stresses may lead to material fatigue, shorten product lifetime, or may even lead to failure (cracking). We have paid attention to keeping the von Mises stress within reasonable limits that would not exceed ~80 MPa, obtained in the simulations for the rectangular cantilever with inertial mass of 4.0 g. This mass value is in accordance with the physical experiment, and is much below cantilever materials' maximum tensile strengths [37] and below PZT-5H bending strength of 114.8 MPa found by Anton et al. [38]. However, when adding an electric circuit simulating the load impedance of 1 MΩ + 50 pF (input impedance of the spectrum analyser [39,40]), the stress is reduced to 78.5 MPa due to the dissipative nature of the electrical resistance that manifests as an equivalent mechanical damping. This stress value was further used in the comparative study evaluating the shapes' performances in same stress conditions.

The current study analyses the behaviour of multilayer piezoelectric structures, fixed constrained at one end and with inertial mass at the free tip. Its original approach consists in emphasizing the generation efficiency with respect to the material volume, not the electric output per se. Our permanent target was the optimum use of the piezoelectric material, by trying to bring all the structures' mechanical stresses to a reference value. The novelty of this study is to address a more valid comparison, maintaining the same mechanical stress in all the shapes to the reference value computed for the rectangular structure, besides investigating the electric response with the same inertial mass. Another approach, that has not been considered in the literature so far, is to evaluate the effectiveness of the piezoelectric material in terms of average voltage and power per unit volume. This reflects much better the impact of material effectiveness in the fixed constrained area on the overall electric output, as well as the less useful free tip material.

We propose a new perspective, considering the increasing costs of piezoelectric materials, as well as sustainability concerns. In this regard, lead zirconate titanate (PZT) piezoceramics [41,42], specifically lead and lead oxide, are classified as hazardous substances within the European Union, planning to restrict their use [43,44]. Lead oxide, a PZT component, is highly toxic, exhibiting even further toxicity enhancement in the manufacturing process [45,46]. However, no other piezoelectric material is yet able to be a competitive substitute for $Pb[Zr_xTi_{1-x}]O_3$ ($0 \leq x \leq 1$), the alternative lead-free materials reaching nowhere near in terms of piezoelectric properties [47] and conversion efficiency. Lead-free piezoelectric materials have begun being studied more thoroughly from the beginning of this century, in response to the environmental concerns, also supported by the impending legislation that was soon to be enforced. Lead-free materials showing good enough piezoelectric properties for energy harvesting include: barium titanate ($BaTiO_3$), zinc oxide (ZnO), potassium niobate ($KNbO_3$), sodium bismuth titanate (BNT), polyvinylidene fluoride (PVFD), aluminium nitride (AlN), nanocrystalline graphene, and other combinations of materials derived from these ones [48–51]. Our paper also comes in response to these restrictions, by showing that better performances can be obtained with structural optimization, encouraging the use of less materials with harmful impact on health and environment.

2. Materials and methods

2.1. Physical piezoelectric transducer

The model which this research is based on started from an available piezoelectric resonant structure for energy harvesting, Midé PPA-4011 (Fig. 1a). The physical PEH is a multilayer cantilever, comprising 17 thin layers (Fig. 1b).

The quadmorph beam's overall dimensions are 71 × 25.4 × 1.32 [mm] (L × W × H) and employs four PZT-5H (lead zirconate titanate) layers (46 × 20.8 × 0.15 [mm]), each of them being sandwiched between two 0.03 mm thick copper electrodes. Five 0.08 mm thick FR4 (flame retardant type 4 glass reinforced epoxy) layers provide insulation and protection. Two of them protect the structure at
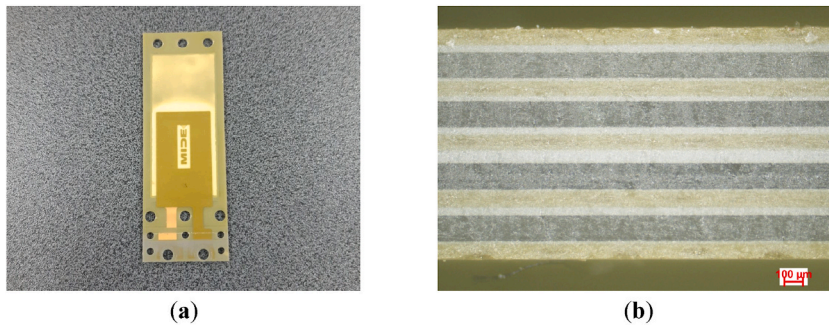
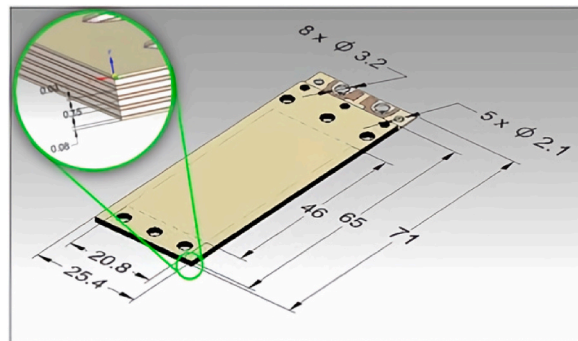**Fig. 1.** (**a**) Midé PPA-4011 piezoelectric harvester; (**b**) side view at electronic microscope.

Fig. 2. CAD model showing the dimensions of the piezoelectric cantilever.

exterior, while the other separate the four sandwiches (copper–PZT-5H–copper), to prevent short-circuits between copper layers [52]. Very thin epoxy films stick together all the layers, but can be discarded in the FEM model (according to product specifications [37]). Epoxy is also used to fill the gaps resulting due to the smaller width and length of piezo layers and copper electrodes.

Fig. 2 shows a 3D CAD (Computer-Aided Design) model designed relying on the dimensions of the physical structure provided in the datasheet [37].

In Table 1, we summarized the material properties of interest provided in the product specifications [37].

The PEH has previously been tested in laboratory [39,53–55] and on a gas turbine test bench [56,57], focusing on the voltage output at resonance. The experimental harvesting system illustrated in Fig. 3 employs the support on which the cantilever is clamped at one end between two bars, and an inertial mass mounted on the free tip, whose elements were weighted at 4.0 g.

Our previous experimental research [39,53], employing the physical rectangular piezoelectric structure, brought us to this paper. We compared the experimental results to the simulation results in Ref. [39], which were validated to a great extent. This allowed us to rely on the digital twin model for rectangular cantilever employed in the paper herein, choosing it as starting point and aiming to improve the structural effectiveness along with reducing the material, and consequently the costs. Experimental results allowed us to validate the numerical simulation results obtained for the rectangular cantilever. The validated model was then used in the shape optimization studies herein.

Table 1
Material properties considered reference values.

No.	Parameter	Symbol	Unit	PZT-5H	Copper	FR4	Structural steel
1.	Piezoelectric strain-charge constants	d_{31}	[C/N $\bullet 10^{-12}$]	−320	N/A	N/A	N/A
		d_{33}	[C/N $\bullet 10^{-12}$]	650	N/A	N/A	N/A
2.	Piezoelectric stress-voltage constants	g_{31}	[V$\bullet$m/N$\bullet 10^{-3}$]	−9.5	N/A	N/A	N/A
		g_{33}	[V$\bullet$m/N$\bullet 10^{-3}$]	19	N/A	N/A	N/A
3.	Density	ρ	[kg/m^3]	7800	8930	1900	7850
4.	Young's modulus	E	[GPa]	63	110	26	200
5.	Mechanical quality factor	Q	ND	30	N/A	N/A	N/A
6.	Relative permittivity	ε	ND	3800	1	4.5	1
7.	Poisson's ratio	υ	ND	0.31	0.343	0.172	0.30
8.	Tensile yield strength	σ	[MPa]	N/A	33.3	340	250
9.	Ultimate tensile yield strength	σ_{max}	[MPa]	60	210	368	400
10.	Curie point	T_C	°C	225	N/A	N/A	N/A
11.	Maximum operating temperature	T_{max}	°C	N/A	1083	130	1400

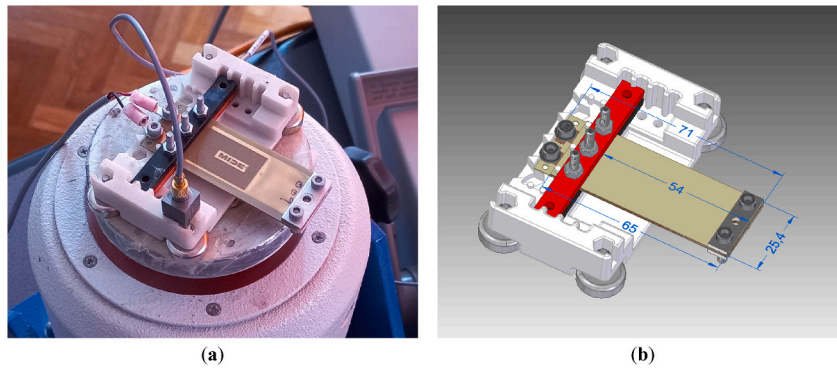*N/A – Not Applicable; ND – Nondimensional.

Fig. 3. (a) Piezoelectric harvesting system on the shaker table and **(b)** CAD model.

The experimental setup (Fig. 4) for testing the original rectangular piezoelectric cantilever, used as reference for the optimizations in the current study, comprises the following elements:

- Stanford SR785 dynamic FFT spectrum analyser [40], able to perform functions generation for driving shaker tables. Its input impedance is 1 MΩ + 50 pF. The ICP (Integrated Circuit Piezoelectric) signal conditioning was activated for our measurements. The amplitude accuracy for frequency response measurement is ±0.2 dB, and the phase accuracy is ±3 deg relative to the external TTL trigger;
- TIRA BAA 120 power amplifier [58] with continuous sine output in RMS power of 120 VA, signal amplification in DC of up to 20 kHz, high signal to noise ratio (SNR >100 dB), and distortion smaller than 0.05 %;
- TIRA S 513 vibration exciter driven by a swept sine signal generated from the spectrum analyser, passed via the power amplifier and connected to the output channel of the analyser. The shaker table has a rated peak force of 100 N, and a frequency range of 2 Hz ÷ 7 kHz, with a maximum acceleration of 45 g [59];
- Piezoelectric energy harvesting system, comprising Midé PPA-4011 piezoelectric harvester, mounted using Midé PPA-9001 clamp kit [37]. The output terminal from the PEH goes into input channel 2 of the analyser via a BNC connector (for the main specifications of the PEH, see Table 1 and Fig. 2);
- Brüel & Kjær 4508-001 triaxial piezoelectric charge accelerometer [60], used for providing a reference input signal. Its sensitivity is 1 mV/m/s^{-2}. The accelerometer is connected to analyser's input channel 1. For ICP accelerometers with a built-in preamplifier, the ICP power supply must be activated for input channel 1 of the analyser.

For the rectangular structure with 4 g inertial mass (see Fig. 3), we obtained 8.356 V/g at a frequency of 118.21 Hz (tests date: 30.08.2023). It is worthwhile to note that, in terms of frequency response and voltage output, differences from the numerical model arise due to several factors that were not considered in the simulations.

First of all, the program simulates in void, hence the friction with air is omitted. Secondly, the unknown elasticity of the clamping method introduced in the experiment by the double-adhesive tape causes extra damping, reflected both on the resonant frequency, as well as on the electric output parameters. The simulated model assumes a perfectly rigid clamping. Thirdly, power losses may occur through cables and cable connections. The spectrum analyser does not have the capability to measure the current.
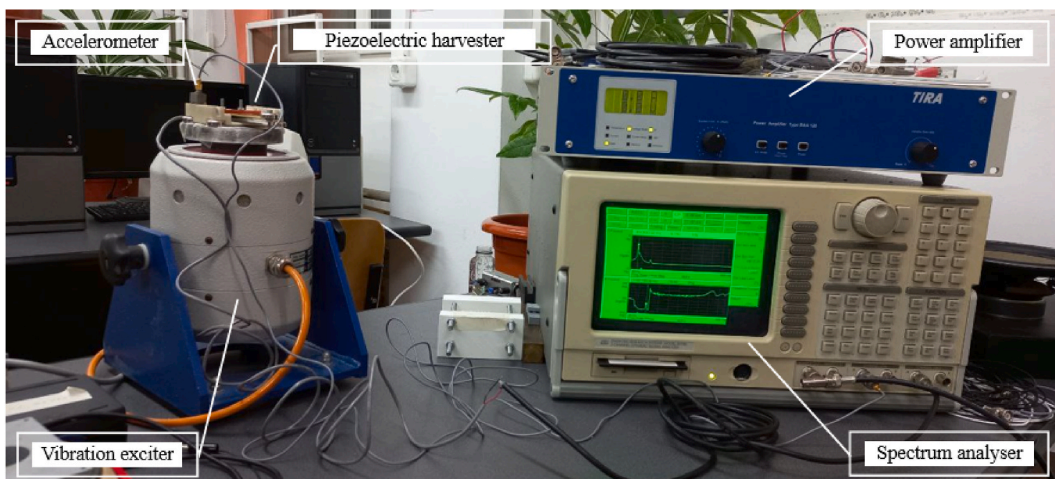

Fig. 4. Experimental laboratory setup (from Ref. [55]).

Measuring the RMS true current with an ammeter would not be reliable, since we would still have no information regarding the values for electric current's real vs. imaginary components, giving the active vs. reactive power. Due to an unknown dephasing between voltage and current introduced by the capacitive components, it is not possible to compute an accurate piezoelectric power output either with the available laboratory equipment.

2.2. Numerical simulations

The numerical simulations sought to replicate the physical properties and experimental conditions as closely as possible, while simplifying the geometry and disregarding the epoxy gluing the layers (according to product specifications [37]), friction with air, as well as the extra damping introduced by the double-sided adhesive tape used for attaching on the shaker. The geometry simplifications included discarding the testing support and all the beam's clamping holes (both the ones for the fixed constraint, as well as the ones for the inertial mass). A perfectly rigid coupling of the clamping bars and tip mass bars was assumed. The considered length in the simulation model was 65 mm (Fig. 5), as the active length in the rear clamp position is of 54 mm. The rest of the beam outside the clamping area can be discarded, as it does not have an influence on the output and there is no piezoelectric material either. All the mass of the inertial mass elements, 4.0 g, was considered within the dimensions and material density of the simulated bars: $25.4 \times 7 \times 1.43$ [mm] (L × W × H) of structural steel with a density of 7866 kg/m^3. The purpose of the work is to assess, in the same simulated conditions, if the shape optimizations render satisfying results by increasing the effectiveness with less piezoceramic material.

The simulations were conducted in COMSOL Multiphysics 6.1, implementing the finite element method (FEM). The steps for building and simulating the model resemble those described by Mota et al. [61]. For a complete evaluation of both mechanical and electrical parameters, Structural Mechanics – Piezoelectric Devices module is employed [62]. The electromechanical behaviour was investigated by interwinding the following physics interfaces:

- **Solid Mechanics**, in which the PZT-5H layers are declared piezoelectric and the initial and boundary conditions are set. An acceleration of 1 g (9.81 m/s^2) is applied on the bottom surface of the lower clamping bar, like in the experiments in our previous research [39]. Mechanical damping [63] is introduced as isotropic loss factor of 0.0333, also calculated in our previous work [39] based on the quality factor found in the datasheet [37]. The default materials properties have been set or modified in the simulation program according to the ones available in the specifications. Mechanical damping was applied, since it is dominant in soft piezoceramic materials like lead zirconate titanate, rendering electrical damping negligeable in no-load conditions.
- **Electrostatics**, where electric charge conservation is set for the piezoelectric layers. Terminals (type electrical circuit) and ground are declared on the faces of the piezo layers, considering that the quadmorph structure connects the four piezoelectric layers similarly to bimorphs, as two sets of pairs. The first two layers act in unison but in the opposite direction to the bottom two layers acting in unison with one another [37]. Therefore, the pairs are connected in series between each other, and the two pairs are electrically in parallel (Fig. 6).
- **Electrical circuit**, for connecting the terminals of the harvester to a load resistance, in order to enable the assessment of both voltage across the load, as well as of the current through the resistor, and hence obtaining information about both the voltage and power generated by the PEH. A resistor-capacitor couple of 1 MΩ + 50 pF, simulating the impedance of the spectrum analyser, was connected in parallel in all the simulations conducted herein.

The piezoelectric constitutive relations connect the mechanical part – mechanical stress and strain, with the electrical part – electric field strength and electric displacement field. The simulation program couples Solid Mechanics and Electrostatics through Multi-
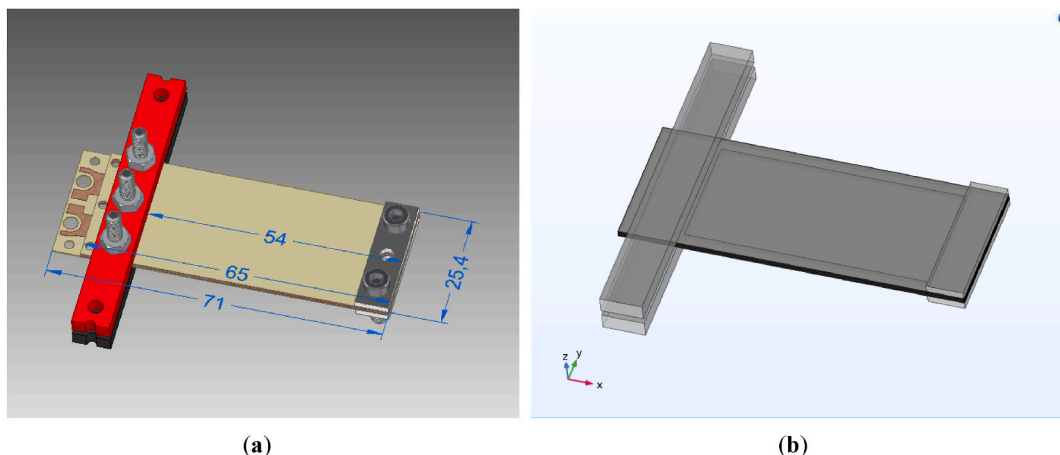

(a)   **(b)**

Fig. 5. (a) CAD model according to reality and **(b)** simulated simplified geometry.
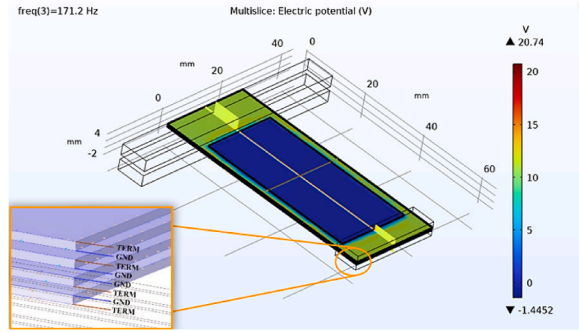
Fig. 6. Electric potential and magnified detail showing how terminals and ground are set.

physics – Piezoelectric effect, which enables a simultaneous numerical solving of all the equations describing solid mechanics and electrostatics, together with the piezoelectric constitutive relations. The strain-charge form was used, given in relation (1) [62]:

$$\begin{cases} \varepsilon_m = s^{\mathbf{E}}\sigma + d^T\mathbf{E} \\ \mathbf{D} = d\sigma + \varepsilon_0\varepsilon_r^T\mathbf{E} \end{cases} \tag{1}$$

where: ε_m [ND] – Strain; $s^{\mathbf{E}}$ [1/Pa] – Elastic compliance, measured in constant electrical field conditions; σ [N/m^2] – Mechanical stress; d [C/N] – Piezoelectric charge constant; d^T [C/N] – Piezoelectric charge constant, measured in constant stress conditions; $\mathbf{E}$ [V/m] – Electric field intensity; $\mathbf{D}$ [C/m^2] – Electric displacement; ε_0 [F/m] – Vacuum permittivity; ε_r^T [F/m] – Relative permittivity, measured under constant stress conditions.

The piezoelectric constitutive relations connect the mechanical part – mechanical stress and strain, with the electrical part – electric field strength and electric displacement field. These relations describing the piezoelectric effect can be expressed in two forms, either in a strain-charge or in a stress-charge form. We are using the strain-charge form herein, since the material data and constants are provided more completely in the strain-charge form. The simulation software can easily make the transformation between one form or the other, so either of the two can be used [62].

When strained, spontaneous electrical polarization occurs in piezoelectric materials. At microscale, the atomic displacements within the unit cell of a deformed solid give birth to electric dipoles. In certain crystalline structures, an average macroscopic dipole moment (electric polarization) mediates the microscopic phenomena [52].

First, a modal analysis was conducted to determine the frequency range that we should consider when studying the frequency domain. This allowed us to reduce computation time and resources by narrowing the frequency range. The modal analysis, as shown in Ref. [62], does not take into account any boundary loads or damping effects, giving the same results whether the acceleration is added or not. The natural frequencies are useful for modal analysis, expressing the frequencies at which the structure is prone to oscillate in absence of any driving force.

In a frequency domain study, almost everything is considered harmonic – from forces and dependent fields to prescribed pressures, displacements, velocities, and accelerations. Frequency domain studies are used for computing the response of a linear or linearized model subjected to a harmonic excitation [62]. The dissipative behaviour of the material can be modelled via complex material properties. Losses of both electrical and mechanical nature can be applied. No default damping is considered except a negligible value depending on the material chosen. At least one damping or loss factor should be manually declared to obtain realistic results [62]. One can either enter hysteretic losses as complex-valued data in equation (1), or loss factor(s) can be declared.

Isotropic loss factor damping is only applicable in eigenfrequency and frequency domain studies. When using loss factor damping, a complex constitutive matrix is used. When an isotropic loss factor η_s is declared, the simulation software uses a matrix of the form in (2). Since we used linear elastic material, this would account to multiplying Young's modulus by $(1 + j\eta_s)$. In other words, complex-valued data can be introduced directly in the fields for material properties, or can be declared as a real-valued material parameter, X, and a set of loss factors, η_X [62], which together form the complex-valued material data in (2).

$$\widetilde{X} = X(1 \pm j\eta_X) \rightarrow \widetilde{Y} = Y(1 \pm j\eta_s) \tag{2}$$

where: X – constitutive matrix computed from material data, $\widetilde{X}$ – complex constitutive matrix used when computing stresses, $j = \sqrt{-1}$ (sign depends on the material property). $X = \mathrm{Re}(\widetilde{X})$; $\eta_X = \mathrm{Im}(\widetilde{X})/\mathrm{Re}(\widetilde{X})$. Y – Young's modulus; η_s – isotropic loss factor.

Thus, the constitutive strain-charge relation of the piezoelectric material used by the simulation program becomes (3):

$$\begin{cases} \varepsilon_m = \widetilde{s}^E\sigma + \widetilde{d}^T\mathbf{E} \\ \mathbf{D} = \widetilde{d}\sigma + \widetilde{\varepsilon}_r^T\mathbf{E} \end{cases} \tag{3}$$

where: $\widetilde{s}^{\mathbf{E}} = (1 - i\eta_{sE})s^{\mathbf{E}}$, $\widetilde{d} = (1 + i\eta_d)d$, $\widetilde{\varepsilon}_r^T = (1 - i\eta_{\varepsilon T})\varepsilon_r^T$ are complex valued matrices, where the imaginary parts represent dissipative functions, with $\eta_X = \eta_{sE}$, η_d, $\eta_{\varepsilon T}$ representing the loss factors associated with each material property.
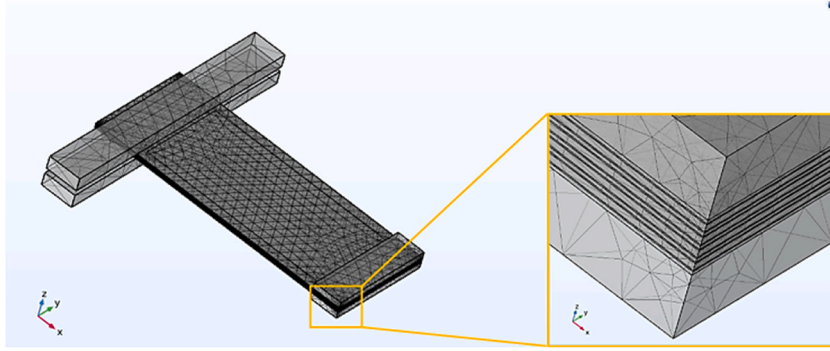
Fig. 7. Tetrahedral mesh elements, with magnified detail on corners and edges.

The frequency domain study renders slightly higher resonance values than the natural frequency computed in the modal analysis study (with about 1 Hz offset). The modal analysis considers only the mechanical problem, the coupling with the electrical circuit being considered in the frequency analysis. The idealized voltage response is assumed to be proportional to the bending speed of the cross-section (spatial derivative of displacement). The frequency response of a system subjected to forced steady-state vibrations if applying acceleration, ω_{acc}, is given by (4) [62]:

$$\omega_{acc} = \omega_n \Big/ \sqrt{1 - 2\zeta^2} \tag{4}$$

where: ω_n [rad/s] – undamped natural angular frequency; ζ [ND] – damping ratio.

It is also useful to provide the well-known relation of the angular frequency and linear natural frequency, together with their dependent parameters, as relation (5) will be addressed, being the computational base of the Eigenfrequency study. The equation from the theory of elasticity is applicable to stratified composite structures. The equivalent Young's modulus is calculated considering the layers thicknesses and moduli of elasticity, and similarly for the cross-section moment of inertia and structure's density [64].

$$f_n = \frac{\omega_n}{2\pi} = \frac{1}{2\pi}\sqrt{\frac{k}{m}} = \frac{1}{2\pi}\sqrt{\frac{\frac{3EI}{L^3}}{m}} \tag{5}$$

where: f_n [Hz] – natural frequency; ω_n [rad/s] – natural pulsation; k [N/m] – equivalent stiffness constant of the composite beam; m [kg] – total beam mass; E [N/m^2] – equivalent Young's modulus of the composite structure; I [kg•m^2] – equivalent moment of inertia of the cross-section; L [m] – beam length.

A complex valued frequency is caused by damping. A complex valued voltage is due to the alternating voltage, with the phase shift being reflected in the imaginary part.

A user-defined mesh was used (Fig. 7), calibrated for coarser tetrahedral elements. This has the advantage of a faster solution, at the cost of some low-quality elements generated that may induce slight inaccuracies in the solution. The mesh has the following parameters: maximum element size: 12.4 mm; minimum element size: 2.6 mm; maximum element growth rate: 1.7; curvature factor: 0.8; narrow regions resolution: 0.3. The tetrahedral mesh is the most suited in our case, as it provides the best balance between accuracy, computational time, convergence rate, and easiness in generating the numerical model [65,66]. A mesh of tetrahedral elements has the advantage of being able to approximate accurately and faster than other mesh geometries the surface contour of our structure with 17 very thin layers [67]. When choosing the physics-controlled mesh, the simulation program assigns tetrahedral elements by default. Our user-defined mesh relied on these aspects, while opting for a coarser size to reduce the computation time, considering the large number of simulations conducted for this paper, especially when assessing the parameters in same mechanical stress conditions and having to modify the inertial mass' density to reach the same stress value after computation.

It is also worth mentioning that we used a direct solver, MUMPS (Multifrontal Massively Parallel Solver), for both modal analysis and frequency domain study. The relative tolerance for the eigenvalue solver was the default 1e-6. For the stationary solver of the frequency domain study, the relative tolerance was increased to 0.1 for all the simulations reported in the paper herein, for the solution to converge without encountering solving errors if the relative error would have been greater than the relative tolerance.

With the above presented information, we set the background for the numerical simulations, the rest being only based on systematic geometry modifications.

3. Results and discussion

3.1. Piezoelectric material reduction towards the tip

A set of numerical simulations was conducted, seeking to gradually reduce the piezoelectric material towards the free tip, as the stress and strain towards the tip gradually decrease to null, from highest value in the fixed constrained area. The domain measurement
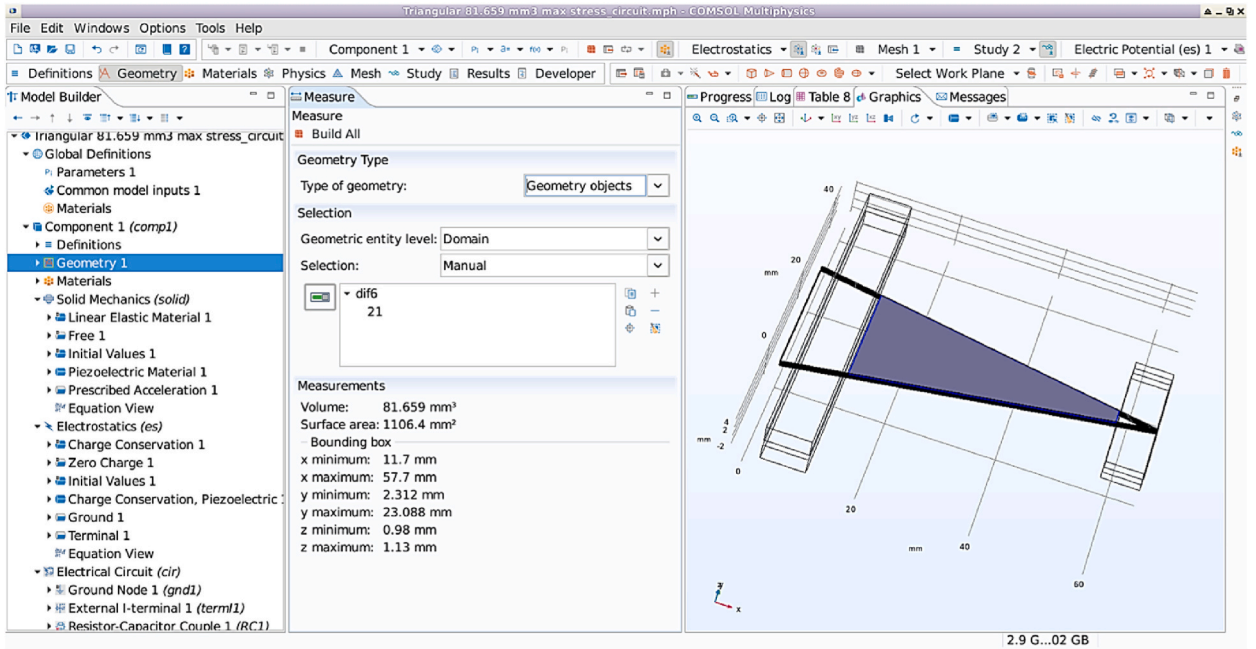
Fig. 8. COMSOL Multiphysics interface and PZT-5H layer volume measurement.

of the volume of one piezoelectric layer for triangular cantilever and the interface of COMSOL Multiphysics are presented in Fig. 8.

The five cases considered in the study started from the rectangular shape, gradually reducing the tip material through three trapezoidal shapes, towards a triangularly sectioned cantilever. The beam length was kept unchanged. The cross-section of the piezoelectric layers at the constrained end was also maintained the same, which can be observed in Fig. 9 below: **(a)** rectangular shape, 143.52 mm^3; **(b)** wide tip trapezoidal, 114.43 mm^3, -20.3 % material; **(c)** medium tip trapezoidal, 108.43 mm^3, -24.4 % material; **(d)** narrow tip trapezoidal, 100.7 mm^3, -29.8 % material; **(e)** triangular, 81.659 mm^3, -43.1 % material.

(a) 143.52 mm^3 **(b)** 114.43 mm^3 **(c)** 108.43 mm^3

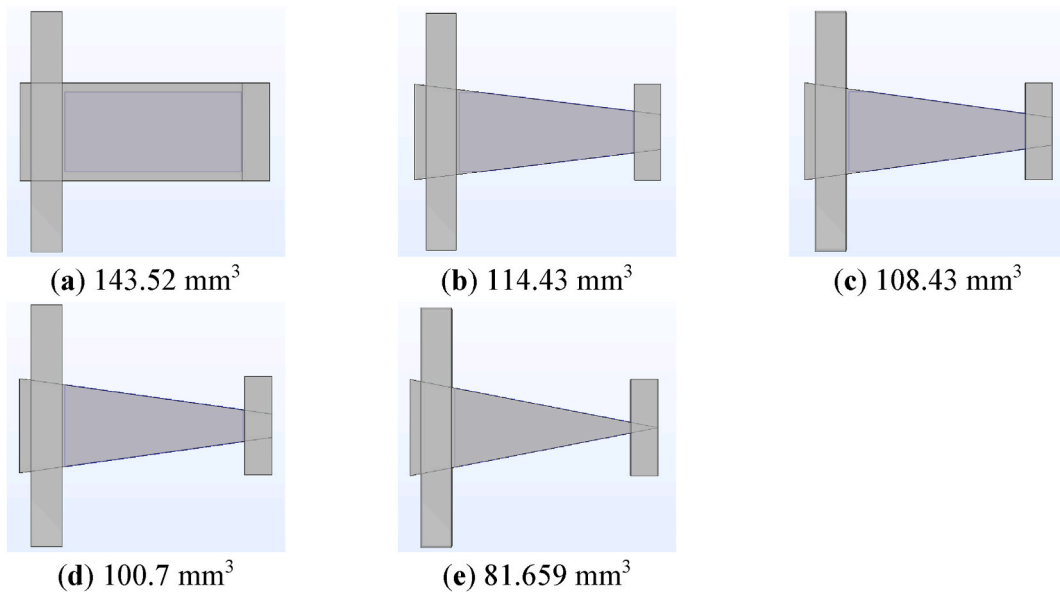**(d)** 100.7 mm^3 **(e)** 81.659 mm^3

Fig. 9. The five cantilever structures studies with their material percentage reductions: **(a)** rectangular; **(b)** trapezoidal, -20.3 %; **(c)** trapezoidal, -24.4 %; **(d)** trapezoidal, -29.8 %; **(e)** triangular, -43.1 %.
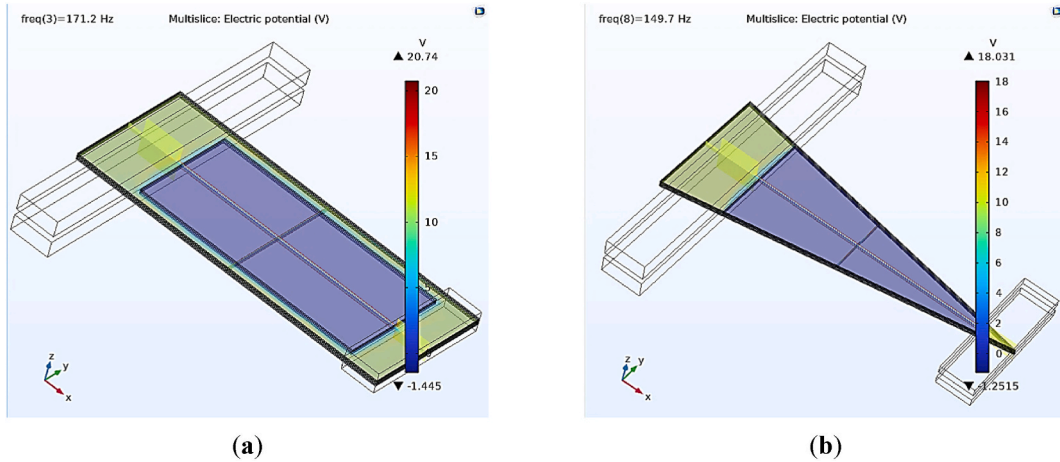
Fig. 10. Electric potential computed at resonance in frequency domain study for **(a)** rectangular cantilever and **(b)** triangular cantilever.

3.1.1. Cantilever with material reduction and same inertial mass

A first set of simulations was conducted with the same inertial mass of 4 g. The tip mass and its shape in the simulations was set so as to match the one used in the experimental tests carried out in our previous work [39] (see Fig. 3). We calculated the tip mass with default structural steel density in COMSOL Multiphysics, $\rho = 7866$ kg/m^3. The length and width of the bars are the same as in experiment, $L \cong 25.4$ mm and $W \cong 7$ mm, and the height was calculated so as to incorporate all the mass elements used, totalling $m = 4$ g. The height of one bar was computed with relation (6).

$$h = \frac{H}{2} = \frac{m}{2 \bullet \rho \bullet L \bullet W} = 1.43 \text{ mm} \tag{6}$$

where: h [mm] – bar height; H [mm] – inertial mass' height; m [g] – inertial mass; ρ [kg/m^3] – inertial mass' density; L [mm] – bar length; W [mm] – bar width.

Captures from the simulation program are presented in Fig. 10, regarding the distribution and maximum values of the electric potential computed numerically for the rectangular vs. triangular cantilevers, at resonant frequency. As one can notice, there is not a great difference in the electric response, of 13 %, while more than 43 % of the piezoelectric material is reduced. This proves that the material in the fixed constrained area is the most effective and reducing it towards the tip does not have a significant impact on the output.

It is interesting to observe the mechanical stress distribution and its maximum value decreasing with ~65 % (Fig. 11) for the triangular shape, down to almost a third of the rectangular cantilever value. This not only means that triangular harvesters produce comparable voltage output at much lower mechanical stress, but also that the expected lifetime can be prolonged if using the same inertial mass, due to subjecting the piezoelectric cantilever to less strain, or that heavier tip masses could be used to boost the electric response even more.
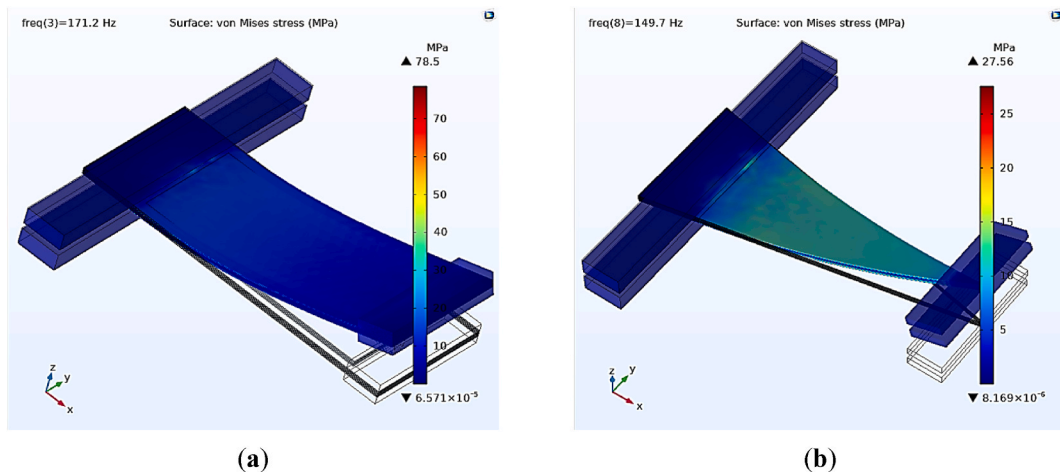

Fig. 11. Von Mises stress computed at resonance in Frequency Domain study for **(a)** rectangular and **(b)** triangular cantilevers.
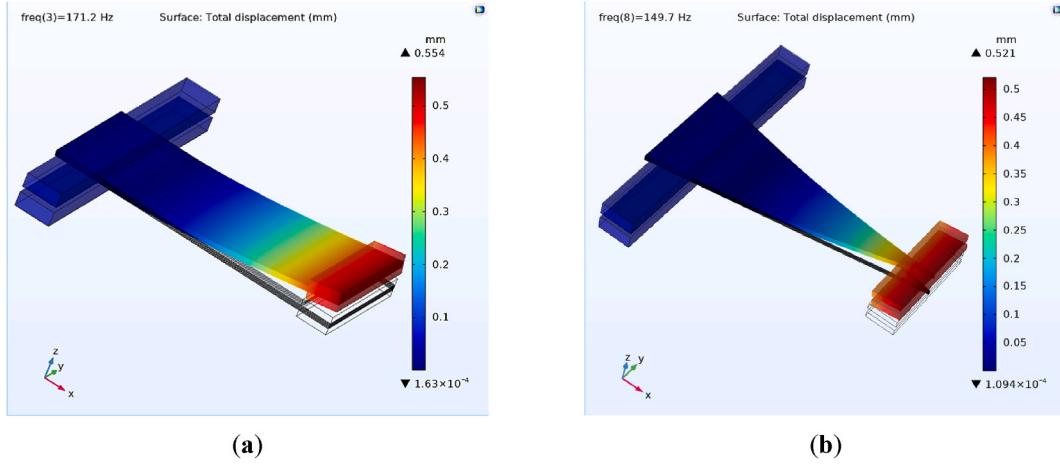
Fig. 12. Total displacement computed at resonance in Frequency Domain study for **(a)** rectangular cantilever and **(b)** triangular cantilever.

The physical explanation for the stress results is that the flexural rigidity is reduced in the case of triangular structure, due to the moment of inertia depending on the beam cross-section. Consequently, the displacement with same inertial mass is lower, due to the higher compliance of the triangular structure. The differences in the total displacement (Fig. 12) are small and comply with the electric potential obtained. The displacement decreases with ~6 % in the triangular case with the same mass of 4 g.

Relying on each value obtained in the frequency domain study for the voltage peak at resonance, V_{pk}, we calculated the average voltage per unit volume of PZT-5H material, V_{avg}. The average voltage per unit volume was calculated as (7):

$$V_{avg} = \frac{V_{pk}}{4 \bullet Vol_{wafer}} \tag{7}$$

where: V_{avg} [V/mm^3] – average voltage; V_{pk} [V] – voltage peak at resonance; Vol_{layer} [mm^3] – layer volume of piezoelectric material.

The power delivered to the load resistor was calculated relying on the power equation (8).

$$P_a = \frac{I_{max}}{\sqrt{2}} \bullet \frac{V_{max}}{\sqrt{2}} = \frac{I_{max} \bullet V_{max}}{2} = 0.5 \bullet I_{max} \bullet V_{max} \tag{8}$$

where: P_a [W] – active power; I_{max} [A] – current amplitude; V_{max} [V] – voltage amplitude.

The expression for active power makes use of the *realdot* operator and is introduced manually in COMSOL Multiphysics, within Results – Derived Values – Global Evaluation. *Realdot* operator treats two complex numbers as real-valued vectors of length 2, returning their dot product [68,69].

In our case, since we used a Resistor-Capacitor Couple (*RC1*), the expression we introduced corresponds to the current and voltage through resistor (*RC1_rcr*), and is written as:

$$0.5 * \text{realdot}(\text{cir.RC1\_rcr\_i}, \text{cir.RC1\_rcr\_v}) \tag{9}$$

(9)

where: cir.RC1_rcr_i [A] – current through resistor; cir.RC1_rcr_v [V] – voltage through resistor.

The *realdot* operator can be regarded as a shorthand form of real(a*conj(b)). However, this expression is not an analytical function of its complex arguments and therefore has no unique partial derivatives with respect to a and b. The difference between realdot(a,b) and real(a*conj(b)) is that the partial derivatives of the former with respect to a and b are defined as conj(b) and conj(a), while for the latter, the partial derivatives are real(b) and real(a). This difference between the partial derivative definitions is important during the sensitivity analysis of frequency response problems. It is therefore recommended that common objective function quantities such as power and energy to be redefined using realdot(a,b) rather than real(a*conj(b)), so that the sensitivity solver to be able to compute correct derivatives [70].

The numerical simulation results for the five cases considered are summarized in Table 2, where: Vol_{piezo_layer} is the PZT-5H volume per layer, Vol_{piezo_total} is the PZT-5H total piezoelectric volume, f_r is the resonant frequency in Frequency Domain study, w is the total displacement, σ_i is the von Mises stress, V_{pk} is the voltage peak at resonance, V_{avg} is the average voltage per unit of material volume, P_r is the active power at resonance, and P_{r_avg} is the average power per unit of material volume. Fluctuations may appear especially due to the number of low-quality mesh elements generated. The relative solution error, *SolEst* has also been extracted from the stationary solver log of the frequency domain study [71].

The data in Table 2 was represented graphically, from rectangular to triangular, through trapezoidal shapes (rhomb markers), the legend representing the material volume of each structure. The curves of the piezoelectric voltage (Fig. 13a) and active power

Table 2

Simulation results for the five beam sections considered, from rectangular to triangular.

| No.	Cantilever section	Vol_{piezo_layer} [mm³]	Vol_{piezo_total} [mm³]	f_r [Hz]	SolEst at f_r [mm]	w [mm]	$σ_i$ [MPa]	V_{pk} [V/g]	V_{avg} [mV/ mm³]	P_r [mW/ g]	P_{r_avg} [μW/ mm³]
1	Rectangular	143.52	574.08	171.2	0.0024	0.554	78.5	20.740	36.127	0.404	0.704
2	Trapezoidal	114.43	457.72	158.5	0.0019	0.492	44.39	16.597	36.260	0.250	0.546
3	Trapezoidal	108.43	433.72	162.0	1.3e-05	0.485	34.06	17.353	40.010	0.273	0.629
4	Trapezoidal	100.7	402.80	152.2	0.0034	0.507	27.60	17.199	42.699	0.270	0.670
5	Triangular	81.659	326.64	149.7	0.0019	0.521	27.56	18.031	55.202	0.300	0.918
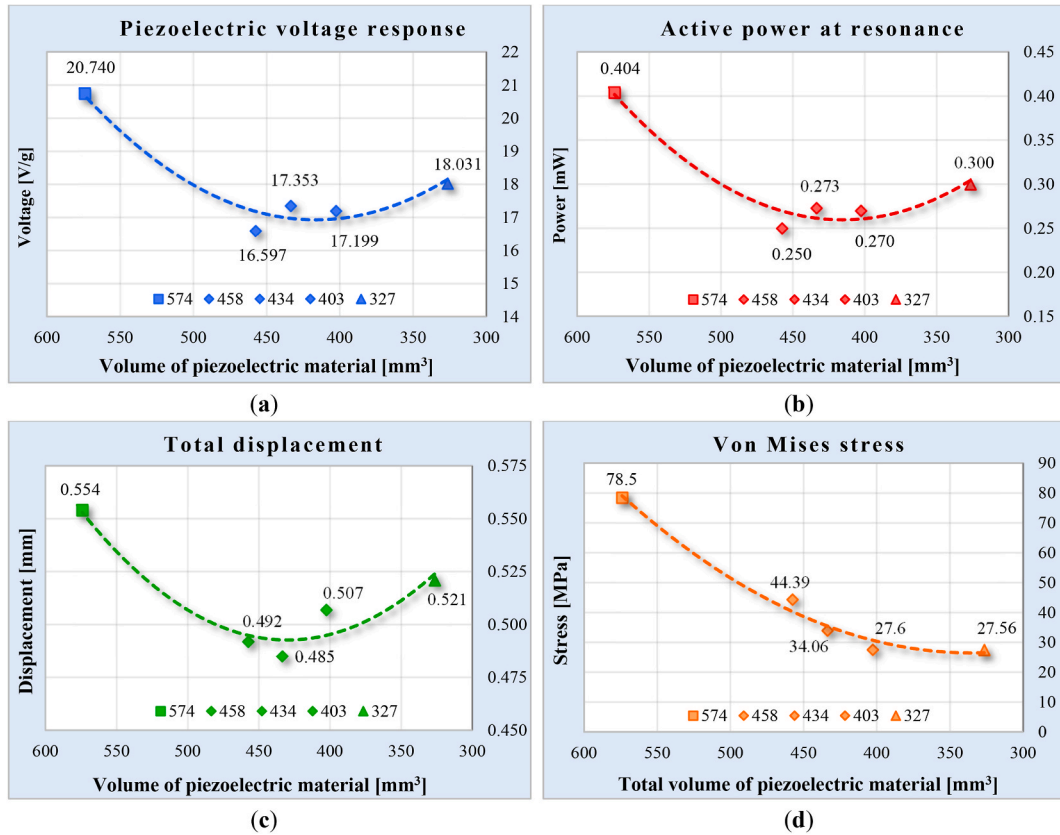
Fig. 13. With same inertial mass: **(a)** Voltage response, **(b)** Active power, at resonant frequency, **(c)** Total displacement, and **(d)** von Mises stress [values obtained at resonant frequency].

(Fig. 13b) are alike, as normal. The total displacement is plotted in Fig. 13c. The horizontal axes were represented with values in reverse order, so that the stress decrease (Fig. 13d) to be easier to grasp and visualize towards the triangular case.

All the values correspond to each structure's resonant frequency. The mechanical stress is reduced by about 65 % from 78.5 MPa (rectangular) to 27.56 MPa (triangular), when using the same mass of 4 g. This is due to the piezoelectric material being most effective in the fixed constrained area, and reducing the less strained material towards the tip not affecting that much the overall voltage and power.

For the structures with same tip mass of 4 g, an increase in voltage per unit volume with almost 53 % is obtained, from 36.127 mV/ mm³ for rectangular cantilever to 55.202 mV/mm³ for triangular structure (Fig. 14a). The power per unit volume, at resonance, increases with 30.4 %, from 0.704 μW/mm³ to 0.918 μW/mm³ (Fig. 14b).

3.1.2. Cantilever with material reduction, maintaining same mechanical stress

Since we observed a stress decrease in the first set of simulations presented above, we deemed worthwhile to conduct a second study, maintaining the same mechanical stress for the five cases ($σ_{i\_ref}$). The simulations were more complex and time demanding, as stress does not have a linear relation with the tip mass, being dependent on the reduced geometry and the moment of inertia of the smaller cross-section as well.
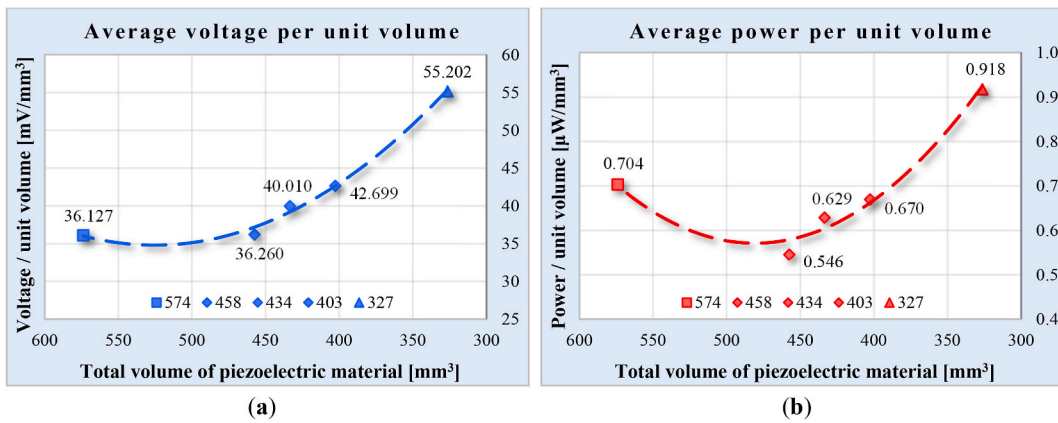
Fig. 14. _With same inertial mass_: **(a)** Average voltage per unit volume, and **(b)** Average power per unit volume.

Table 3
Parameters obtained for the five beam shapes, in same stress conditions.

No.	Cantilever section (Vol_{piezo_layer})	Piezo layer volume	m_i [g]	ρ_i [kg/m³]	f_r [Hz]	SolEst at f_r	w [mm]	$\sigma_{i\,ref}$ [MPa]	V_{pk} [V/g]	V_{avg} [mV/mm³]	P_r [mW/g]	P_{r_avg} [μW/mm³]
1	Rectangular (574.08 mm³)	143.52	4	7866	171.2	0.0024	0.554	78.5	20.740	36.127	0.404	0.704
2	Trapezoidal (457.72 mm³)	114.43	8.78	17262	113.6	0.0040	0.886	78.5	30.032	65.612	0.872	1.905
3	Trapezoidal (433.72 mm³)	108.43	11.81	23216.5	100.4	0.0055	1.141	78.5	40.961	94.441	1.704	3.929
4	Trapezoidal (402.80 mm³)	100.7	14.75	29000	84.5	0.0069	1.475	78.5	50.208	124.647	2.551	6.333
5	Triangular (326.64 mm³)	81.659	13.42	26400	84	0.0066	1.510	78.5	52.172	159.725	2.580	7.899

Some prior calculations were done, considering a certain linearity, relying on relation (10), to have a starting value for mass. Only the density of the tip mass material was varied, according to the corresponding mass required to reach the same mechanical stress, σ_{ref}, of 78.5 MPa, considered maximum reference of the rectangular structure with 4 g tip mass. The shape and dimensions of the tip mass were kept unchanged for a relevant comparison and for not introducing further unknown variables, influencing the results interpretation.

$$\rho_i = \frac{m_i}{L \bullet W \bullet H} = \frac{m \bullet \frac{\sigma_{ref}}{\sigma_i}}{L \bullet W \bullet H} \tag{10}$$

where: ρ_i [kg/m³] – density for required mass; m_i [g] – inertial mass for 78.5 MPa; L [mm] – length; W [mm] – width; H [mm] – height; m [g] – initial mass (4 g); σ_{ref} [MPa] – reference stress (78.5 MPa); σ_i [MPa] – stress (see Table 2); i – iteration parameter for cases 1 ÷ 5.

The numerical results for the five cantilever shapes at constant mechanical stress are summarized in Table 3, where $\sigma_{i\,ref}$ is the target stress achieved for every new iteration.

We found that, in same stress conditions, the displacement increases about 3 times (Fig. 15c), due to the reduced bending stiffness. The supported inertial mass (Fig. 15d) increases about 3.3 times for triangular shape compared to the traditional rectangular cantilever, rendering more than 2.5 times higher voltage output (Fig. 15a), and almost 6.4 times power increase (Fig. 15b).

The triangular cantilever has a much lower resonance frequency due to a higher supported mass compared to the rectangular beam. Consequently, the displacement and the voltage output of the triangular cantilever are much larger, resulting in a higher output power.

The plots in Fig. 16 compare the average voltage per unit volume of piezoelectric material, while maintaining the same mechanical stress at 78.5 MPa, as in the original rectangular cantilever case. A very significant material effectiveness improvement is obtained. The voltage per unit volume (Fig. 16a) records an increase of ~342 %, from 36.127 mV/mm³ (rectangular) to 159.725 mV/mm³ (triangular) in same stress conditions. At the same time, the increase in power per unit volume (Fig. 16b) is quite remarkable, with 1022 %, from 0.704 μW/mm³ in rectangular case to 7.899 μW/mm³ in triangular case with material cutdown.

3.2. Optimum resistive load for maximum power

In order to grasp the maximum power that can be achieved by piezoelectric harvesters with shape optimization, a frequency domain study was conducted, with an auxiliary parametric sweep of the resistor. The capacitance value of 50 pF was kept the same in
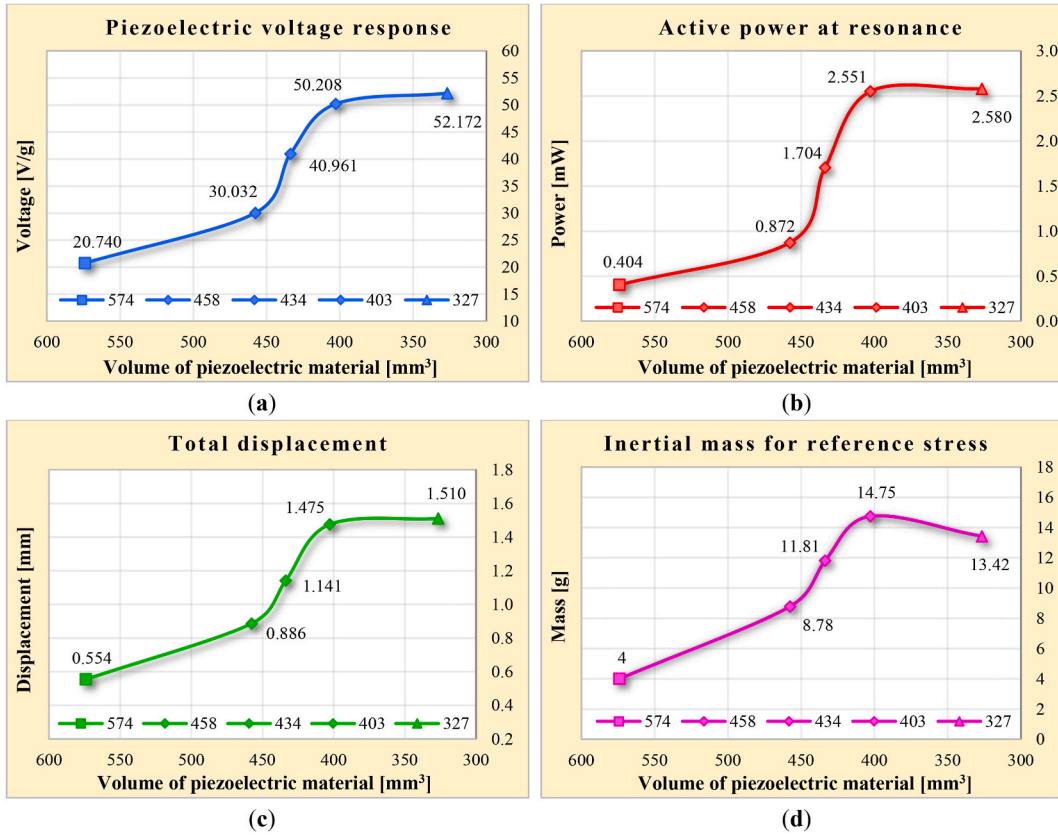
Fig. 15. <u>In same stress conditions</u>: **a)** Voltage response, **(b)** Power output, **(c)** Total displacement, **(d)** Tip mass required for achieving 78.5 MPa stress [values at resonance].

all the simulations, while the load dependence was assessed by sweeping the load resistance. It is worth mentioning that the load dependence frequency domain study was ran with the default relative tolerance of 0.001 for the stationary solver, as the solution errors were small enough.

The piezoelectric structure is capacitive by nature, hence the external capacitor introduces a 90 deg phase shift between capacitor current and voltage, if the capacitance dominates in the circuit. Due to this dephasing, the reactive part increases very much, and the active dissipated power becomes very small compared to the reactive power. Ideally, the load should be purely resistive, but in real applications it is very difficult to avoid using external capacitors in the circuitry required for piezoelectric harvesters. Nevertheless, in our case, the resistive part dominates at the low operation frequency of the harvester, rendering the capacitance negligible. The resonant frequency is much below the cutoff frequency expressed as (11). This means that the spectrum analyser's impedance of 1 MΩ in parallel with 50 pF acts as a lowpass filter with a cutoff frequency of 3.183 kHz.

$$f_C = \frac{\omega_C}{2\pi} = \frac{1}{2\pi RC} \tag{11}$$

where: f_C [Hz] – cutoff frequency; ω_C [rad/s] – cutoff angular frequency; R [Ω] – external load resistance; C [F] – external capacitance.

Practically, we only have active power, as the reactive power is negligeable due to the working (resonant) frequency being much below the cutoff frequency. Due to the high resistance of 1 MΩ, the maximum power is not found exactly at the mechanical resonance where maximum stress and maximum voltage occur, but slightly lower (with 0.8 Hz). The problem of load optimization for maximum power is very complex and depends on the parameters of the external circuit. However, matching the resistance improves the power to a great extent, as demonstrated by the studies hereinafter.

Observing from the above results that the triangular beam is the most effective, we assessed the matching load for maximum power output. The optimal resistive load was evaluated for the rectangular structure, triangular with same mass of 4 g, and triangular at same stress of 78.5 MPa, showing that the power is maximum at a resistance with almost two orders of magnitude below the 1 MΩ of the spectrum analyser used in laboratory experiments (see Fig. 17).

The electromechanical coupling coefficient was also extracted from the simulation program, using relation (12).

$$k_{eff}^{2} = \frac{\text{Electrical energy stored}}{\text{Mechanical energy applied}} \Rightarrow k_{eff} = \sqrt{\frac{\text{es.intWe}}{\text{solid.Ws\_tot}}} \tag{12}$$
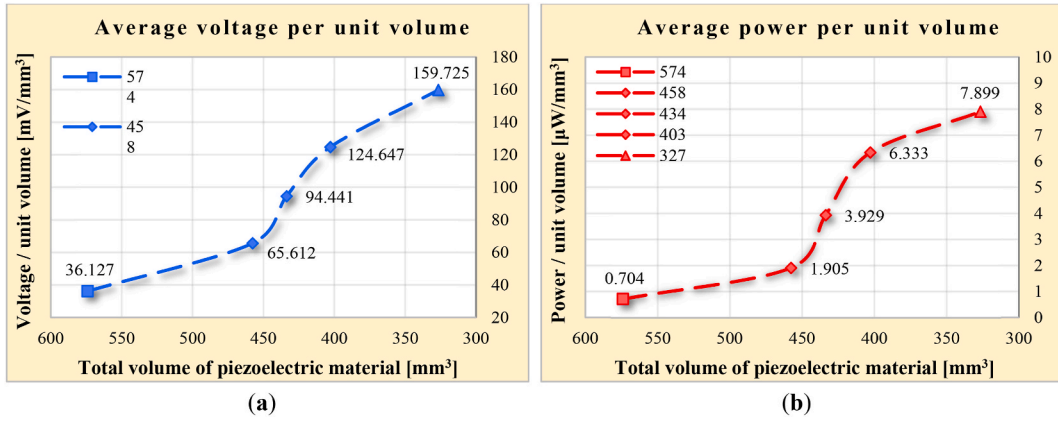
Fig. 16. <u>In same stress conditions</u>: **(a)** Average voltage per unit volume, **(b)** Average power per unit volume, from rectangular to triangular shape.

(a) Rectangular   **(b)** Triangular, same mass   **(c)** Triangular, same stress
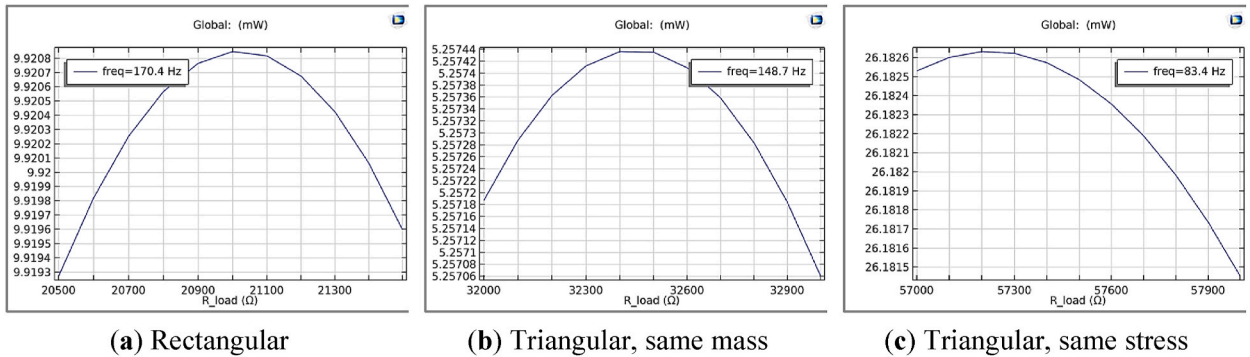
Fig. 17. Load dependence of the three evaluated cases.

Table 4
Simulation results for maximum power with optimum resistive load.

No.	Cantilever section (Vol_{piezo_layer})	Vol_{piezo_total} [mm³]	m_i [g]	ρ_i [kg/m³]	f_r [Hz]	f_{P_max} [Hz]	SolEst at f_{P_max}	P_{a_max} [mW]	R_{load_opt} [kΩ]	P_{MAX_opt} [mW]	$V_{P\_max\_abs}$ [V]	k_{eff} [ND]
1	Rectangular, (143.52 mm³)	574.08	4	7866	171.2	170.4	1.2e-05	0.797	21.0	9.921	20.413	0.27053
2	Triangular, same mass (81.659 mm³)	326.64	4	7866	149.7	148.7	1.8e-06	0.638	32.4	5.257	35.715	0.26731
3	Triangular, same stress (81.659 mm³)	326.64	13.42	26400	84	83.4	3.5e-07	5.358	57.2	26.183	54.777	0.26958

where: k_{eff} [ND] – electromechanical coupling coefficient; es.intWe [W] – total electric energy; solid.Ws_tot [W] – total elastic strain energy.

The numerical results for the three cases considered are summarized in Table 4, where: f_{P_max} is the frequency corresponding to maximum power (slightly lower than the resonance frequency, f_r); P_{RMS_max} is the maximum RMS power for 1 MΩ + 50 pF load, at f_{P_max}; R_{load_opt} is the optimized resistive load; P_{MAX_opt} is the maximized power with R_{load_opt}; $V_{P\_max\_abs}$ is the voltage corresponding to P_{MAX_opt}; and k_{eff} is the electromechanical coupling coefficient.

The differences between the coupling coefficients for the three cases are negligible, rendering a conversion efficiency of about 27 %. The maximized power outputs for matching resistance (P_{MAX_opt}) record a great increase compared to using the analyser impedance (P_{RMS_max}), as follows: ~1145 % increase for rectangular beam, ~724 % for triangular with same mass, and a ~389 % increase for triangular structure at same stress). These results actually show that the spectrum analyser's impedance is almost two orders of magnitude above the optimal load for these piezoelectric cantilevers. This study is of great importance for future experiments outside laboratory, before choosing the electric circuitry for piezoelectric energy harvesting.
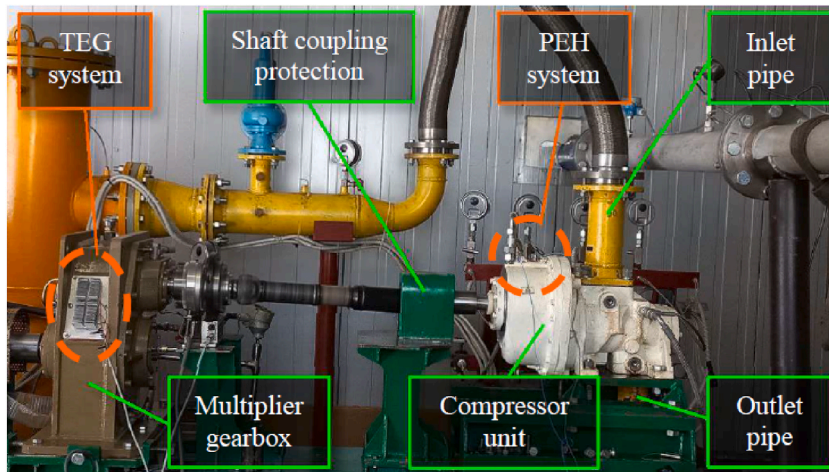
Fig. 18. Compressor test bench.

3.3. Applicability in industrial environment and economic considerations

Future research will pursue the experimental validation of the simulation results. We aim further than laboratory conditions, to test the piezoelectric harvesters in relevant industrial environment, on a twin-screw compressor available on test bench (see Fig. 18). A more extensive impedance matching for maximizing the power output shall also be conducted, taking into account the circuitry elements required for piezoelectric energy harvesting (such as an energy harvesting demo circuit like LTC3588-1 or a custom-made rectifying circuit for more PEHs). A study for matching the piezoelectric resonant frequency with the target frequency source shall be addressed as well. However, the measuring system should not be a conventional one, as all oscilloscopes have the standard input resistance of 1 MΩ.

Wireless sensor networks (WSNs), together with structural health monitoring (SHM), have been vehiculated for the last two decades as an ultimate application for piezoelectric harvesters (PEH), without much progress outside laboratories ideal conditions. We are conducting preliminary experimental works on a twin-screw compressor, aiming to validate and bring the piezoelectric energy harvesting with the acquired rectangular structure at a higher technology readiness level (TRL). The experiments aim for an industrially relevant environment (TRL 6), namely a test bench for industrial compressors [72]. The piezoelectric harvester's resonant frequency has to be adjusted in real-time to match the male rotor frequency targeted, of ~83 Hz [55]. The piezoelectric harvesters are envisaged as part of a multisource harvesting system, along with thermoelectric generators (TEGs) harnessing the heat.

However, the power output from a single device is not enough to power a WSN circuitry. In the industrial environment we are dealing with space constraints, and we must also consider other factors such as prolonging the lifetime of the piezoelectric harvesters at higher working temperatures. All these aspects, along with the continuously rising costs of piezoelectric ceramics, make the harvesters' replacement an economically infeasible solution. For reference, we provided in Table 5 the comparative pricing of PZT-based harvesters from the same manufacturer, between 2017 and 2024. The data was taken from products specifications [37,73].

Even though piezoelectric energy harvesting has met significant advancements within the past decade, the research on energy harvesters has been mostly conducted without aiming for specific applications, and without considering the environmental conditions, the solution reliability, and the feasibility of the harvesting system integration. Potential real-world applications that could benefit from the shape optimization presented herein include powering portable or wearable health monitoring devices, such as pacemakers and shoes, tire pressure monitoring systems, and structural health monitoring for industrial machinery, buildings and bridges [74].

Cutting the piezoceramic material almost down to half would make piezoelectric harvesters more affordable. Implementing the proposed triangular piezoelectric cantilevers would boost manufacturers' sales and would encourage the research and development. For example, a destructive test or assessing the parameters that may lead to depolarization would not seem that intangible. The paper

Table 5
Price evolution for similar piezoelectric harvesters from the same manufacturer.

Harvester	PPA-4011	S452-J1FR-1808XB	PPA-2011	S230-J1FR-1808XB	PPA-1011	S128–H5FR-1107 YB	S128-J1FR-1808 YB
Number of active layers	4	4	2	2	1	1	1
Piezoelectric material	PZT-5H	PZT-5J	PZT-5H	PZT-5H	PZT-5H	PZT-5H	PZT-5J
Sensitivity at resonance [V/g]	3	3	6	6	4.3	3	4
Power at rated g [mW]	1.4	1.4	1.2	1.2	0.7	0.4	0.7
Year	2017	2024	2017	2024	2017	2024	2024
Price	$300	$832.48	$238.00	$663.08	$200	$283.14	$292.82

shows that it is less important how much material is used, but what matters is using the material in an optimized way. Two triangular harvesters could be manufactured using the same material volume of a rectangular structure, which would be more cost and power effective.

4. Conclusions

The present study outlines that a triangular structure with less material towards the free tip makes use of the piezoelectric material more effectively in terms of average voltage and power generated per unit volume. Also, stress is reduced from rectangular to triangular structures, making it possible to withstand heavier inertial masses, which would furthermore increase efficiency. Hence, we also conducted a study maintaining the same von Mises stress, in which we observed the voltage and power per unit volume of PZT-5H.

These evaluations are new studies that show a more valid comparison regarding shape optimization. The most effective shape proved to be the triangular shape with material reduction towards the tip. We report a 53 % increase in voltage per unit volume and 30.4 % in power per unit volume for the triangular cantilever with same mass, compared to the traditional rectangular cantilever. In the same stress conditions, the triangular structure exhibits a 342 % increase in voltage per unit volume and a 1022 % increase in power per unit volume, compared to the rectangular shape. This further comes with the advantage of reducing the material with more than 43 %.

Our paper brings several novelty elements compared to the current literature regarding shape optimization. We investigated not only the electric response with an inertial tip mass, but also addressed a more valid comparison between the shapes, maintaining the same mechanical stress as in the rectangular structure. Another approach, that has not been considered in the existent literature, is evaluating the effectiveness of the piezoelectric material in terms of average voltage and power per unit volume. This reflects more clearly the impact of the material effectiveness in the fixed constrained area on the average electric output, as well as the less useful free tip material. A triangular or trapezoidal section transducer would provide a more cost-effective solution as well, by reducing the piezoelectric material that does not produce significant electric output. Hence, it would be more efficient to use the same amount of material split into two triangular transducers instead of one rectangularly shaped.

CRediT authorship contribution statement

Claudia Săvescu: Writing – review & editing, Writing – original draft, Visualization, Validation, Software, Project administration, Methodology, Investigation, Formal analysis, Data curation, Conceptualization. **Daniel Comeagă:** Writing – review & editing, Validation, Supervision, Conceptualization. **Adrian Stoicescu:** Writing – review & editing, Resources, Formal analysis.

Declaration of competing interest

The authors declare that they have no known competing financial interests or personal relationships that could have appeared to influence the work reported in this paper.

References

[1] S.R. Anton, M. Safaei, Piezoelectric energy harvesting, in: A.-G. Olabi (Ed.), Encyclopedia of Smart Materials, Elsevier, Oxford, 2022, pp. 104–116, https://doi.org/10.1016/B978-0-12-815732-9.00044-9.

[2] S. Sriphan, T. Charoonsuk, T. Maluangnont, N. Vittayakorn, Piezoelectric energy harvesting for low-power smart electronics, in: A.S.M.A. Haseeb (Ed.), Encyclopedia of Materials: Electronics, Academic Press, Oxford, 2023, pp. 369–404, https://doi.org/10.1016/B978-0-12-819728-8.00050-4.

[3] M.R. Rashmi, K. Trilok Sairam, A. Suresh, Energy harvesting through piezoelectric technology, Mater. Today: Proc. (2023), https://doi.org/10.1016/j.matpr.2023.07.252.

[4] S. Panda, S. Hajra, K. Mistewicz, P. In-na, M. Sahu, P.M. Rajaitha, et al., Piezoelectric energy harvesting systems for biomedical applications, Nano Energy 100 (2022) 107514, https://doi.org/10.1016/j.nanoen.2022.107514.

[5] Y. Veli, A.M. Morega, An energy harvesting device for portable applications, UPB Scientific Bulletin, Series C: Electr. Eng. 83 (2021) 199–206.

[6] J. Song, G. Zhao, B. Li, J. Wang, Design optimization of PVDF-based piezoelectric energy harvesters, Heliyon 3 (2017) e00377, https://doi.org/10.1016/j.heliyon.2017.e00377.

[7] Z. Yu, Y. Wu, Z. Fang, H. Sun, Modeling and compensation of hysteresis in piezoelectric actuators, Heliyon 6 (2020) e03999, https://doi.org/10.1016/j.heliyon.2020.e03999.

[8] S. De Caro, R. Montanini, S. Panarello, A. Quattrocchi, T. Scimone, A. Testa, A PZT-based energy harvester with working point optimization. 2017 6th International Conference on Clean Electrical Power, ICCEP), 2017, pp. 699–704, https://doi.org/10.1109/ICCEP.2017.8004767.

[9] K. Chen, S. Fang, Q. Gao, D. Zou, J. Cao, W.-H. Liao, Enhancing power output of piezoelectric energy harvesting by gradient auxetic structures, Appl. Phys. Lett. 120 (2022) 103901, https://doi.org/10.1063/5.0082015.

[10] M. Ashford, B. Onyenucheya, J. Zirnheld, K. Burke, Improving a piezoelectric energy harvester output using a synchronized switch harvesting Design. 2021 IEEE Pulsed Power Conference (PPC), 2021, pp. 1–5, https://doi.org/10.1109/PPC40517.2021.9733126.

[11] D. Zhu, S. Beeby, J. Tudor, N. White, N. Harris, Improving output power of piezoelectric energy harvesters using multilayer structures, Procedia Eng. 25 (2011) 199–202, https://doi.org/10.1016/j.proeng.2011.12.049.

[12] S. Paquin, Y. St-Amant, Improving the performance of a piezoelectric energy harvester using a variable thickness beam, Smart Mater. Struct. 19 (2010) 105020, https://doi.org/10.1088/0964-1726/19/10/105020.

[13] S. Sunithamani, P. Lakshmi, Flora E. Eba, PZT length optimization of MEMS piezoelectric energy harvester with a non-traditional cross section: simulation study, Microsyst. Technol. 20 (2014) 2165–2171, https://doi.org/10.1007/s00542-013-1920-y.

[14] E. Zulueta, E. Kurt, Y. Uzun, J.M. Lopez-Guede, Power control optimization of a new contactless piezoelectric harvester, Int. J. Hydrogen Energy 42 (2017) 18134–18144, https://doi.org/10.1016/j.ijhydene.2017.01.180.

[15] M. Edla, Y.Y. Lim, D. Mikio, R.V. Padilla, A single-stage rectifier-less boost converter circuit for piezoelectric energy harvesting systems, IEEE Trans. Energy Convers. 37 (2022) 505–514, https://doi.org/10.1109/TEC.2021.3103879.

[16] A.M. Matos, J.M. Guedes, K.P. Jayachandran, H.C. Rodrigues, Computational model for power optimization of piezoelectric vibration energy harvesters with material homogenization, Comput. Struct. 192 (2017) 144–156, https://doi.org/10.1016/j.compstruc.2017.07.015.

[17] A.A. Hashim, K.I. Mahmoud, H.M. Ridha, Geometry and shape optimization of piezoelectric cantilever energy harvester using COMSOL Multiphysics software, International Review of Applied Sciences and Engineering 12 (2021) 103–110, https://doi.org/10.1556/1848.2021.00170.

[18] S.A. Kouritem, K.T. Mohamed, A.M.N. Elmekawy, H. Elgamal, Optimization methodology to target a vibration source natural frequency of energy harvesting cantilever. Ninth International Conference on Advances in Civil, Structural and Mechanical Engineering - ACSM, 2019, 2019, pp. 19–25, https://doi.org/10.15224/978-1-63248-173-3-04.

[19] S.A. Kouritem, W.A. Altabey, Ultra-broadband natural frequency using automatic resonance tuning of energy harvester and deep learning algorithms, Energy Convers. Manag. 272 (2022) 116332, https://doi.org/10.1016/j.enconman.2022.116332.

[20] L. Shang, C. Hoareau, A. Zilian, Optimal electrode coverage based on a new criterion for piezoelectric energy harvesters, Energy Convers. Manag. 284 (2023) 116982, https://doi.org/10.1016/j.enconman.2023.116982.

[21] J. Wang, B. Fan, J. Fang, J. Zhao, C. Li, A piezoelectric energy harvester based on multi-cantilevers and magnetic force, Energy Rep. 8 (2022) 11638–11645, https://doi.org/10.1016/j.egyr.2022.09.005.

[22] J.-X. Wang, J.-C. Li, W.-B. Su, X. Zhao, C.-M. Wang, A multi-folded-beam piezoelectric energy harvester for wideband energy harvesting under ultra-low harmonic acceleration, Energy Rep. 8 (2022) 6521–6529, https://doi.org/10.1016/j.egyr.2022.04.077.

[23] A. Moayedizadeh, D. Younesian, Application of the meta-substrates for power amplification in rotary piezoelectric energy harvesting systems: Design, fabrication and testing, Energy Rep. 8 (2022) 5653–5667, https://doi.org/10.1016/j.egyr.2022.04.022.

[24] A. Pasharavesh, H. Dalir, Flexural modes coupling in cantilever-type piezoelectric energy harvesters, Energy Rep. 7 (2021) 6438–6450, https://doi.org/10.1016/j.egyr.2021.09.109.

[25] Y. Li, P. Yan, A compliant mechanism based piezoelectric beam energy harvester with multi-mode frequency up conversion, Energy Rep. 10 (2023) 932–940, https://doi.org/10.1016/j.egyr.2023.07.044.

[26] Z.S. Chen, Y.M. Yang, G.Q. Deng, Analytical and experimental study on vibration energy harvesting behaviors of piezoelectric cantilevers with different geometries. 2009 International Conference on Sustainable Power Generation and Supply, 2009, pp. 1–6, https://doi.org/10.1109/SUPERGEN.2009.5348290.

[27] K. Mohamed, H. Elgamal, S.A. Kouritem, An experimental validation of a new shape optimization technique for piezoelectric harvesting cantilever beams, Alex. Eng. J. 60 (2021) 1751–1766, https://doi.org/10.1016/j.aej.2020.11.024.

[28] H. Salmani, G.H. Rahimi, S.A. Hosseini Kordkheili, An exact analytical solution to exponentially tapered piezoelectric energy harvester, Shock Vib. 2015 (2015) e426876, https://doi.org/10.1155/2015/426876.

[29] X. Dong, Z. Yi, L. Kong, Y. Tian, J. Liu, B. Yang, Design, fabrication, and characterization of bimorph micromachined harvester with asymmetrical PZT films, J. Microelectromech. Syst. 28 (2019) 700–706, https://doi.org/10.1109/JMEMS.2019.2920213.

[30] D. Benasciutti, L. Moro, S. Zelenika, E. Brusa, Vibration energy scavenging via piezoelectric bimorphs of optimized shapes, Microsyst. Technol. 16 (2010) 657–668, https://doi.org/10.1007/s00542-009-1000-5.

[31] V.J. Caetano, M.A. Savi, Multimodal pizza-shaped piezoelectric vibration-based energy harvesters, J. Intell. Mater. Syst. Struct. 32 (2021) 2505–2528, https://doi.org/10.1177/1045389X211006910.

[32] H. Li, D. Liu, J. Wang, X. Shang, M.R. Hajj, Broadband bimorph piezoelectric energy harvesting by exploiting bending-torsion of L-shaped structure, Energy Convers. Manag. 206 (2020) 112503, https://doi.org/10.1016/j.enconman.2020.112503.

[33] Z. Xie, L. Liu, W. Huang, R. Shu, S. Ge, Y. Xin, et al., A multimodal E-shaped piezoelectric energy harvester with a built-in bistability and internal resonance, Energy Convers. Manag. 278 (2023) 116717, https://doi.org/10.1016/j.enconman.2023.116717.

[34] W. Wang, J. Huang, Z. Yao, Cut-corner prism piezoelectric energy harvester based on galloping enhancement mechanism, Energy Rep. 7 (2021) 6366–6374, https://doi.org/10.1016/j.egyr.2021.09.081.

[35] C. Borzea, D. Comeagă, Y. Veli, A. Săvescu, Piezoelectric cantilever harvester with trapezoidal/triangular section for increased conversion efficiency. Iberian COMSOL Multiphysics Conference 2022, 2022, pp. 54–57.

[36] J. Baker, S. Roundy, P. Wright, Alternative geometries for increasing power density in vibration energy scavenging for wireless sensor networks, in: 3rd International Energy Conversion Engineering Conference, American Institute of Aeronautics and Astronautics, San Francisco, California, 2005, https://doi.org/10.2514/6.2005-5617.

[37] Midé Technology, PPA PRODUCTS Datasheet & User Manual, 2017. https://cdn2.hubspot.net/hubfs/3841176/Data-Sheets/ppa-piezo-product-datasheet.pdf.

[38] S.R. Anton, A. Erturk, D.J. Inman, Bending strength of piezoelectric ceramics and single crystals for multifunctional load-bearing applications, IEEE Trans. Ultrason. Ferroelectrics Freq. Control 59 (2012) 1085–1092, https://doi.org/10.1109/TUFFC.2012.2299.

[39] C.I. Borzea, C.D. Comeagă, A. Săvescu, Boosting the electric output of a cantilever piezoelectric harvester by tip curvature blocking elements. 8th European Conference on Renewable Energy Systems (ECRES 2020), 2020, pp. 344–350.

[40] Stanford Research Systems, Dynamic signal analyzer - SR785 n.d. https://www.thinksrs.com/downloads/pdfs/catalog/SR785c.pdf. (Accessed 6 June 2023).

[41] D. Hidayat, M. Taufik, S. Setianto, One-step synthesis of lead zirconate titanate particles using a solid-state reaction method, Heliyon 8 (2022) e09125, https://doi.org/10.1016/j.heliyon.2022.e09125.

[42] H. Zhai, Y. Jiang, H. Li, P. Zhang, Y. He, D. Shi, et al., In situ polarization and dielectric property measurements of Pb(Zr0.52Ti0.48)O3 ferroelectric nanocrystals, Heliyon 3 (2017) e00313, https://doi.org/10.1016/j.heliyon.2017.e00313.

[43] T. Takenaka, H. Nagata, Current status and prospects of lead-free piezoelectric ceramics, J. Eur. Ceram. Soc. 25 (2005) 2693–2700, https://doi.org/10.1016/j.jeurceramsoc.2005.03.125.

[44] E. Ringgaard, T. Wurlitzer, Lead-free piezoceramics based on alkali niobates, J. Eur. Ceram. Soc. 25 (2005) 2701–2706, https://doi.org/10.1016/j.jeurceramsoc.2005.03.126.

[45] P.K. Panda, Review: environmental friendly lead-free piezoelectric materials, J. Mater. Sci. 44 (2009) 5049–5062, https://doi.org/10.1007/s10853-009-3643-0.

[46] Y. Wu, H. Zhang, Y. Zhang, J. Ma, D. Xie, Lead-free piezoelectric ceramics with composition of (0.97−x)Na1/2Bi1/2TiO3-0.03NaNbO3-xBaTiO3, J. Mater. Sci. 38 (2003) 987–994, https://doi.org/10.1023/A:1022333427521.

[47] M.A. Ahmad, A. Allataifeh, Electrical extraction of piezoelectric constants, Heliyon 4 (2018) e00910, https://doi.org/10.1016/j.heliyon.2018.e00910.

[48] B. Malič, M. Otoničar, K. Radan, J. Koruza, Lead-free piezoelectric ceramics, in: M. Pomeroy (Ed.), Encyclopedia of Materials: Technical Ceramics and Glasses, Elsevier, Oxford, 2021, pp. 358–368, https://doi.org/10.1016/B978-0-12-803581-8.12131-9.

[49] Nor N. Mohamad, H.H. Hamzah, K. Abdul Razak, Chapter 9 - recent advancement in sustainable energy harvesting using piezoelectric materials, in: K. Y. Cheong, L.-C. Chen (Eds.), Sustainable Materials for Next Generation Energy Devices, Elsevier, 2021, pp. 221–248, https://doi.org/10.1016/B978-0-12-820628-7.00009-5.

[50] H. Khanbareh, A. Rasheed, J. Khaliq, 13 - piezoelectric composites, in: K. Asadi (Ed.), Organic Ferroelectric Materials and Applications, Woodhead Publishing, 2022, pp. 457–475, https://doi.org/10.1016/B978-0-12-821551-7.00014-2.

[51] T. Takenaka, 4 - lead-free piezo-ceramics, in: K. Uchino (Ed.), Advanced Piezoelectric Materials, Woodhead Publishing, 2010, pp. 130–170, https://doi.org/10.1533/9781845699758.1.130.

[52] C. Borzea, A. Morega, D. Comeagă, Y. Veli, Temperature influence on the performances of a PZT-5H piezoelectric harvester. 2021 12th International Symposium on Advanced Topics in Electrical Engineering (ATEE), IEEE, Bucharest, Romania, 2021, pp. 1–6, https://doi.org/10.1109/ATEE52255.2021.9425102.

[53] C.I. Borzea, C.D. Comeagă, M.N. Uddin, R.D. Hrițcu, V.L. Ringheanu, Improving the electric response of a cantilever piezoelectric energy harvester by constraining tip curvature, IOP Conf. Ser. Mater. Sci. Eng. 997 (2020) 012038, https://doi.org/10.1088/1757-899X/997/1/012038.

[54] C. Borzea, D. Comeagă, Adjusting the resonant frequency of a cantilever piezoelectric harvester, Scientific Journal TURBO V (2018) 11–18.

[55] C. Săvescu, D. Comeagă, A. Morega, Y. Veli, Experimental tests with piezoelectric harvester for tuning resonant frequency to vibrating source, Rev. Roumaine Sci. Tech. - Ser. Électrotech. Énerg. 67 (2022) 457–460.

[56] C. Borzea, D. Comeagă, A. Stoicescu, C. Nechifor, Piezoelectric harvester performance analysis for vibrations harnessing, UPB Scientific Bulletin, Series C: Electr. Eng. 81 (2019) 237–248.

[57] A. Stoicescu, M. Deaconu, H. Romeo, C. Nechifor, V. Vilag, Vibration energy harvesting potential for turbomachinery applications, INCAS BULLETIN 10 (2018) 135–148, https://doi.org/10.13111/2066-8201.2018.10.1.13.

[58] TIRA GmbH,. Technical Parameters Amplifier BAA 120 2023. https://www.tira-gmbh.de/fileadmin/inhalte/download/schwingprueftechnik/verstaerker/analog/EN/data_sheet_BAA_120_V03.pdf.

[59] B. Ambrożkiewicz, Z. Czyż, P. Karpiński, P. Stączek, G. Litak, Ł. Grabowski, Ceramic-based piezoelectric material for energy harvesting using hybrid excitation, Materials 14 (2021) 5816, https://doi.org/10.3390/ma14195816.

[60] Brüel, Kjær. PRODUCT DATA CCLD Accelerometer Types 4507 and 4508, CCLD TEDS Accelerometer Types 4507-B and 4508-B, Charge Accelerometer Types 4507-C and 4508-C, Dec. 2012. http://www.octsources.com/otcadmin/document/pdf/20170424/1493021891.pdf.

[61] B.C. Mota, B.A. Neto, S.H.A. Barroso, F.T.S. Aragão, A.J.L. Ferreira, J.B. Soares, et al., Characterization of piezoelectric energy production from asphalt pavements using a numerical-experimental framework, Sustainability 14 (2022) 9584, https://doi.org/10.3390/su14159584.

[62] COMSOL, Structural Mechanics Module User's Guide, 2022. Version: COMSOL 6.1, https://doc.comsol.com/6.1/doc/com.comsol.help.sme/StructuralMechanicsModuleUsersGuide.pdf.

[63] H. Sönnerlind, Damping in Structural Dynamics: Theory and Sources, COMSOL, 2019. https://www.comsol.com/blogs/damping-in-structural-dynamics-theory-and-sources/. (Accessed 30 March 2024).

[64] C.I. Borzea, C.D. Comeagă, Reliability of euler-Bernoulli model for multilayer composite piezoelectric beams. 2019 11th International Symposium on Advanced Topics in Electrical Engineering (ATEE), 2019, pp. 1–6, https://doi.org/10.1109/ATEE.2019.8724964.

[65] Fairclough C. Efficiently Mesh Your Model Geometry with Meshing Sequences. COMSOL n.d. https://www.comsol.com/blogs/efficiently-mesh-your-model-geometry-with-meshing-sequences/(accessed March 27, 2024).

[66] Hexahedral mesh vs. Tetrahedral: comparing high-quality meshing n.d. https://resources.system-analysis.cadence.com/blog/msa2022-hexahedral-mesh-vs-tetrahedral-comparing-high-quality-meshing. (Accessed 27 March 2024).

[67] P. Mehmert, Chapter Eleven - residual stress analysis and geometrical tolerances in powder bed fusion and direct energy deposition processes, in: J. Kadkhodapour, S. Schmauder, F. Sajadi (Eds.), Quality Analysis of Additively Manufactured Metals, Elsevier, 2023, pp. 429–486, https://doi.org/10.1016/B978-0-323-88664-2.00014-2.

[68] COMSOL. Piezoelectric Energy Harvester, Created in COMSOL Multiphysics, 2022. https://www.comsol.com/model/download/1072791/models.mems.piezoelectric_energy_harvester.pdf.

[69] C. Hu, K. Behdinan, R. Moradi-Dastjerdi, PVDF energy harvester for prolonging the battery life of cardiac pacemakers, Actuators 11 (2022) 187, https://doi.org/10.3390/act11070187.

[70] COMSOL, COMSOL Multiphysics Reference Manual, 2022. Version: COMSOL 6.1, https://doc.comsol.com/6.1/doc/com.comsol.help.comsol/COMSOL_ReferenceManual.pdf. (Accessed 30 March 2024).

[71] COMSOL. The Log Window. DocComsolCom n.d. https://doc.comsol.com/6.1/doc/com.comsol.help.comsol/comsol_ref_solver.35.105.html (accessed April 2, 2024).

[72] C. Săvescu, V. Petrescu, D. Comeagă, I. Vlăducă, C. Nechifor, F. Niculescu, Vibration analysis of a twin-screw compressor as a potential source for piezoelectric energy harvesting, Rev. Roumaine Sci. Tech. - Ser. Électrotech. Énerg. 68 (2023) 253–258, https://doi.org/10.59277/RRST-EE.2023.3.1.

[73] PIEZO.COM. Piezoelectric Energy Harvesters. PIEZOCOM n.d. https://piezo.com/collections/piezoelectric-energy-harvesters (accessed April 10, 2024).

[74] Z. Yang, S. Zhou, J. Zu, D. Inman, High-performance piezoelectric energy harvesters and their applications, Joule 2 (2018) 642–697, https://doi.org/10.1016/j.joule.2018.03.011.